Eng., Univ. Wisconsin, Eng. Expt. Sta. Rept. 3, Madison (1955).
Maslov, P. G., "Certain Physical Characteristics of Alkyl Derivatives of Benzene," *Doklady Akademii Nauk SSSR*, **132**, 1156 (1960).
Mathur, B. C., S. H. Ibrahim, and N. R. Kuloor, "New Simple Correlation Predicts Critical Temperature," *Chem. Eng.*, **76**, (6), 182 (1969).
Nokay, R., "Estimate Petrochemical Properties," *ibid.*, **66** (4), 147 (1959).
Ogle, G. J., and P. I. Gold, "Estimating Thermophysical Properties of Liquids, Part 2—Critical Properties," *ibid.*, **75**, (11), 185 (1968).
Reid, R. C., and T. K. Sherwood, *The Properties of Gases and Liquids*, 2nd Edit., pp. 6-44, McGraw-Hill, New York (1966).
Reidel, L., "Eine Neue Universelle Dampfdrunchformel," *Chem. Ing.-Tech.*, **26**, 83 (1954).
———., "Berechnung der Kritischen Daten der verzweigten Paraffin-Kohlenwasserstoffe," *ibid.*, **35**, 433 (1963).
Viswanath, D. S., "Ideal Critical Volume as a Correlating Parameter, *Brit. Chem. Eng.*, **13**, 532 (1968).

Manuscript received August 2, 1972; revision received November 24 and accepted November 27, 1972.

Computation of Three-Dimensional Viscous Flow Between Convergent Traveling Surfaces

The Marker-and-Cell numerical technique has been adapted to develop a method of solution for three-dimensional, unconfined, isothermal flow of a highly viscous, Newtonian fluid in a region bounded by two, nonparallel traveling surfaces. Results are reported only for plane and elliptical surfaces, but the analysis is general enough to handle any shape of interest.

A computer program was developed which can be used to generate and plot the flow and pressure fields. Numerical results were obtained for the special case of symmetrically opposed convergent surfaces for a wide range of conditions.

EDDY A. HAZBUN
and
STUART W. CHURCHILL

School of Chemical Engineering
University of Pennsylvania
Philadelphia, Pennsylvania 19104

SCOPE

A computer program was developed for prediction of the transient and steady flow of a highly viscous fluid between two wide, symmetrically opposed traveling surfaces. This method of forming plastic sheet is asserted by Bortnick et al. (1970) to be superior to the conventional system of fixed extruder die and takeoff rollers. The fluid is introduced between the moving surfaces as a jet as indicated in Figure 1. It undergoes changes in pressure and velocity that are governed by the volumetric rate of flow, the properties of the fluid, and the vertical spacing, velocity, and curvature of the traveling surfaces. The fluid is assumed to be Newtonian, incompressible, and isothermal.

The distinguishing characteristics of this process are the free boundaries of the fluid and the three-dimensionality. The process is described in terms of a mathematical model which is based on the general differential equations for the conservation of mass and momentum. A functional dependence is postulated for the variation of the velocity components in the vertical direction, and the resulting two-dimensional equations are solved numerically in the unsteady state using a modified form of the Marker-and-Cell method to keep track of the boundaries of the fluid. This is one of the most complex problems of flow that has yet been solved. It involves complexities not previously encountered with the Marker-and-Cell method. Hence the development of the general method of solution is described in considerable detail. The finite-difference representation which is more conventional is not described in detail.

The objective of the study has been to develop a method for prediction of the behavior of polymer melts during the forming of sheets. The investigation covers a range of flow conditions of practical interest and two configurations for the traveling surface.

CONCLUSIONS AND SIGNIFICANCE

Results in the form of tabulations and plots of the transient velocity and pressure fields were obtained directly from the computer. Typical results for two representative cases, one for convergent surfaces and the other for elliptical convergent surfaces, are presented in Figures 5 to 16. The conditions for these two cases are summarized in Table 2. Figure 5 shows the location of fluid particles at a series of times for the first case. Such plots could be projected in sequence to simulate the motion of the fluid. The location of the free boundary at a series of times

Correspondence concerning this paper should be addressed to S. W. Churchill. E. A. Hazbun is with Rohm and Haas Company, c/o Lennig Chemicals, Port Clarence, Teesside, England.

is shown in Figures 6 and 11 for the two cases. Numerical values for the pressure and velocity fields are given in Figures 7 to 10 and 12 to 16.

The force of the entering jet and the drag of the traveling surfaces convey the fluid forward. The generated pressure causes the fluid to spread transversely until a terminal width is attained. The detailed behavior is seen to be very complex.

The results provide the basis for the mechanical design of equipment for the formation of plastic sheets. The details of the velocity field are important since they determine the quality of the sheets.

The development is for a Newtonian fluid. However, the results are expected to be a good approximation for many non-Newtonian fluids under practical conditions, using the effective viscosity at zero rate of strain.

Numerical convergence was established by performing the calculations for several grid sizes. The grid size used for the bulk of the computations yields values within 6% of the values obtained by extrapolating the grid size to zero.

The industrial processing of highly viscous polymer melts involves geometrically complex equipment such as screw extruders, extrusion dies, calenders, spinnerets, and injection molds. The designer of such equipment is confronted with a dilemma posed on the one hand by the complex rheological behavior of these fluids and on the other hand by the mathematical difficulties encountered in attempting to integrate the related transient equations of motion for nontrivial configurations. The inclusion of a shear-dependent viscosity is as difficult as it is important for the accurate characterization of the flow (McIntire and Showalter, 1972). The proper design of industrial equipment requires analysis of the flow in the true geometry of interest rather than in a grossly simplified system. The combined general problem is beyond current mathematical and computational capabilities. Therefore, the design engineer must choose one of the following alternatives:

1. Simplify the mechanical configuration but select an accurate constitutive equation.
2. Assume Newtonian flow but consider the true geometry.
3. Follow an intermediate approach by considering a reasonable approximation of the configuration and a simple non-Newtonian model.

Although a great deal of attention has been given to the problem of relating the shear stress to the rate of deformation of polymer melts, a simple but generally applicable constitutive equation has yet to emerge. The difficulties encountered in such studies have diverted serious analysis away from the real flow systems in which polymer melts are handled commercially. Fortunately, these systems are often operated over a sufficiently limited range of low velocities so that the dependence of viscosity on shear rate can be neglected without significant error. That is, although the material is non-Newtonian, the effective viscosity at zero rate of shear can be used as a reasonable approximation for the finite rates of shear which are encountered. For this reason, the second alternative was followed in this study.

Figure 1 is a generalized representation of the plastic sheet forming section of a commercial system (Bortnick et al., 1970). A jet (A) of highly viscous material is introduced between two wide, symmetrically opposed, and initially convergent traveling surfaces (S1 and S2). The fluid adheres to the moving surfaces and is conveyed in the x-direction by a combination of shear and inertia. At the same time, the generated pressure causes the fluid stream to spread laterally (in the y-direction) under isothermal conditions until a terminal width is reached as the moving surfaces become parallel. Further downstream, the belts become parallel, and the continuously formed melt sheet is cooled and frozen allowing it to separate from the belts. The location of the unconfined surface of the fluid is not known a priori. The velocity distributions developed within the fluid determine the alignment of the polymer molecules and hence to a large extent the quality of the sheet which is produced. The pressure profiles which are generated govern the mechanical structure of the equipment. Hence, by investigating the effect of parameters such as the curvature of the convergent section, the speed of the belts, the sheet thickness, the sheet width, the flow rate and the fluid viscosity, sufficient information is generated to allow the construction of a workable system.

This method for forming plastic sheet is asserted by Bortnick et al. to be superior to the conventional fixed extruder die and take-off rollers process for the following reasons:

1. Since the polymer melt adheres to the traveling surfaces, all defects in the plastic sheet caused by friction against the fixed surfaces of an extruder die are eliminated.
2. The long cooling section of parallel belts allows controlled gradient cooling of the melt to yield plastic sheet of isotropic characteristics superior to sheet finished on the conventional take-off and polishing rollers.
3. By avoiding the processing step in which the melt issuing from a slit die is transferred to a pair of take-off rollers, all problems associated with die swell and uneven flow distribution across the die are eliminated.
4. When molten polymers of high molecular weights are forced through a fixed slit die at desirable production rates, large back pressures are generated which create instabilities in the fluxing and pumping equipment and result in serious defects in the sheet called *flow lines* or *nerve*. In the proposed system, the pumping equipment is isolated from the sheet forming equipment and the pressures developed are minimized due to the absence of fixed

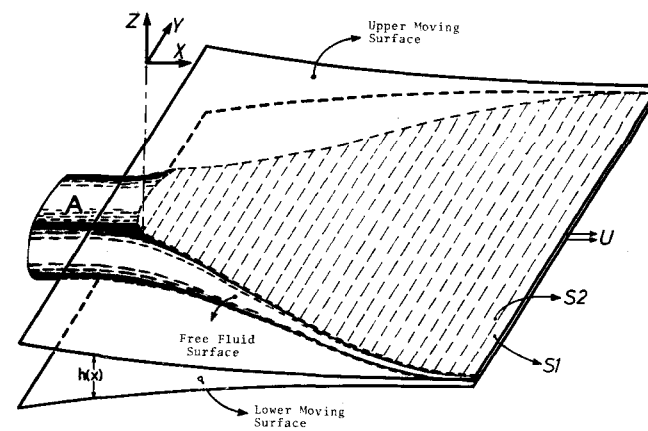

Fig. 1. Configuration of the problem.

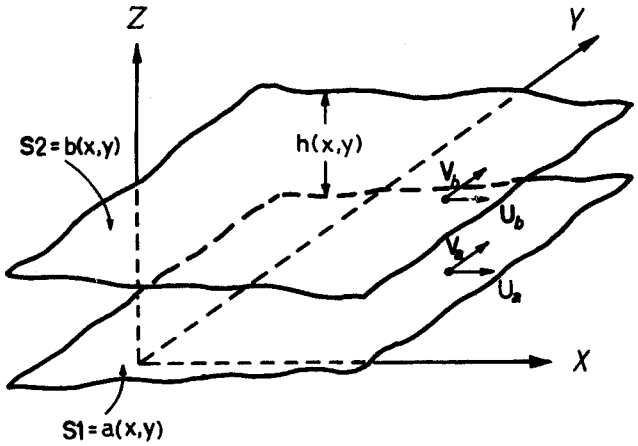

Fig. 2. Bounding surfaces, generalized case.

surfaces and the ability to distribute uniformly the work load throughout the convergent section of the flexible belts.

Two cases of different curvature are presented in this paper principally to illustrate the numerical solution.

MATHEMATICAL FORMULATION

General Case

Starting with the Navier-Stokes equations, a mathematical model is developed to simulate the incompressible Newtonian flow in a region bounded by two nonparallel moving surfaces using a three-dimensional extension of the two-dimensional treatment employed by Amsden and Harlow (1970). The equations of continuity and transport of momentum may be vectorially represented by

$$\nabla \cdot \vec{V} = 0 \tag{1}$$

and

$$\frac{\partial \vec{V}}{\partial t} + \nabla \cdot (\vec{V}\vec{V}) = -\nabla\Phi + \nu\nabla^2\vec{V} + \vec{g} \tag{2}$$

At the two moving surfaces S1 and S2 shown in Figure 2, the mass flux is zero, that is,

$$\frac{Da}{Dt} = \frac{Db}{Dt} = 0 \tag{3}$$

Hence at the lower surface where $z = a$

$$w = u\frac{\partial a}{\partial x} + v\frac{\partial a}{\partial y} \tag{4}$$

and at the upper surface where $z = b$

$$w = u\frac{\partial b}{\partial x} + v\frac{\partial b}{\partial y} \tag{5}$$

To confine the flow within the bounding surfaces, Equations (1) and (2) are expressed in terms of the Cartesian velocity components u, v, and w and integrated from $z = a$ to $z = b$. Equations (4) and (5) are then substituted in the resulting expressions. Equation (1) reduces to

$$\frac{\partial}{\partial x}\int_a^b u\,dz + \frac{\partial}{\partial y}\int_a^b v\,dz = 0 \tag{6}$$

The three components of the Equation (2) transform to

$$\frac{\partial}{\partial t}\int_a^b u\,dz + \frac{\partial}{\partial x}\int_a^b u^2\,dz + \frac{\partial}{\partial y}\int_a^b uv\,dz =$$
$$-\int_a^b \frac{\partial\phi}{\partial x}\,dz + \nu\int_a^b \left(\frac{\partial^2 u}{\partial x^2} + \frac{\partial^2 u}{\partial y^2}\right)dz$$
$$+\nu\left[\left(\frac{\partial u}{\partial z}\right)_{z=b} - \left(\frac{\partial u}{\partial z}\right)_{z=a}\right] + g_x \tag{7}$$

$$\frac{\partial}{\partial t}\int_a^b v\,dz + \frac{\partial}{\partial x}\int_a^b uv\,dz + \frac{\partial}{\partial y}\int_a^b v^2\,dz =$$
$$-\int_a^b \frac{\partial\phi}{\partial y}\,dz + \nu\int_a^b \left(\frac{\partial^2 v}{\partial x^2} + \frac{\partial^2 v}{\partial x^2}\right)dz$$
$$+\nu\left[\left(\frac{\partial v}{\partial z}\right)_{z=b} - \left(\frac{\partial v}{\partial z}\right)_{z=a}\right] + g_y \tag{8}$$

and

$$\frac{\partial}{\partial t}\int_a^b w\,dz + \frac{\partial}{\partial x}\int_a^b uw\,dz + \frac{\partial}{\partial y}\int_a^b vw\,dz =$$
$$-\int_a^b \frac{\partial\phi}{\partial z}\,dz + \nu\int_a^b \left(\frac{\partial^2 w}{\partial x^2} + \frac{\partial^2 w}{\partial y^2}\right)dz$$
$$+\nu\left[\left(\frac{\partial w}{\partial z}\right)_{z=b} - \left(\frac{\partial w}{\partial z}\right)_{z=a}\right] + g_z \tag{9}$$

Equations (6) to (9) are rigorous consequences of Equations (1) and (2) but in this form are not amenable to general solution.

Simplification for Smoothly Curved Moving Surfaces

If the analysis is limited to the practical case in which the flexures of the bounding surfaces S1 and S2 are relatively small in magnitude, the functional dependence of the field variables on the vertical space variable z may be approximated as

$$u(x, y, z, t) \equiv u(x, y, t) \cdot f(z) + \frac{(z-a)U_b + (b-z)U_a}{(b-a)} \tag{10}$$

and

$$v(x, y, z, t) \equiv v(x, y, t) \cdot f(z) + \frac{(z-b)V_b + (b-z)V_a}{(b-a)} \tag{11}$$

For the case of noslip walls moving parallel to themselves and not changing shape, $f(z)$ is a parabolic function vanishing at the walls, and U_a, U_b, V_a and V_b are functions of x and y only.

Using Equations (10) and (11), the integrals in Equations (6) to (9) can be evaluated. To obtain a convenient frame of reference, $f(z)$ can be equated to unity on some surface that lies between the bounding surfaces; on this surface $u(x, y, t)$ and $v(x, y, t)$ are the actual velocity components. To avoid specifying $f(z)$, $a(x, y)$ and $b(x, y)$ at this stage the following entities are defined:

$$h(x, y) = b(x, y) - a(x, y) \tag{12}$$

$$r(x, y) = \int_a^b f(z)\,dz \tag{13}$$

$$s(x, y) = \int_a^b f(z)^2\,dz \tag{14}$$

$$R_u = \int_a^b f(z)\left[\frac{(z-a)V_b + (b-z)U_a}{h}\right]dz \tag{15}$$

$$R_v = \int_a^b f(z)\left[\frac{(z-a)V_b + (b-z)V_a}{h}\right]dz \tag{16}$$

$$\alpha = f'(b) - f'(a) \tag{17}$$

Starting with Equation (6), u and v are replaced with the right-hand side terms of Equations (10) and (11) and the integral terms are evaluated yielding

$$\frac{\partial ur}{\partial x} + \frac{\partial vr}{\partial y} + MBC = 0 \tag{18}$$

The term MBC reflects the movement of the two surfaces and is defined as

$$MBC = \frac{\partial}{\partial x}\left[\frac{h}{2}(U_b + U_a)\right] + \frac{\partial}{\partial y}\left[\frac{h}{2}(V_b + V_a)\right] \tag{19}$$

The integration of Equations (7) and (8) is rather lengthy; the right-hand sides of Equations (10) and (11) are again substituted for u and v, each term is then integrated with respect to z. Whenever the integral of $f(z)$ appears, it is replaced by one of the definitions in Equations (12) to (17). The momentum equations transform to

$$\frac{\partial ur}{\partial t} + \frac{\partial u^2 s}{\partial x} + \frac{\partial uvs}{\partial y} = -h\frac{\partial \phi}{\partial x} + \nu r\left(\frac{\partial^2 u}{\partial x^2} + \frac{\partial^2 u}{\partial y^2}\right) + \nu u\alpha + g_x + MBX \tag{20}$$

where

$$MBX = -\frac{\partial}{\partial x}\left\{\frac{h}{3}(U_b^2 + U_bU_a + U_a^2)\right\} - \frac{\partial}{\partial x}(2uR_u) - \frac{\partial}{\partial y}\left\{\frac{h}{6}(2U_bV_b + U_bV_a + V_bU_a + 2U_aV_a)\right\} - \frac{\partial}{\partial y}(uR_v + vR_u) + \nu\left[\left\{\frac{\partial^2}{\partial x^2} + \frac{\partial^2}{\partial y^2}\right\}\left\{\frac{h}{2}(U_b + U_a)\right\}\right] \tag{21}$$

and

$$\frac{\partial vr}{\partial t} + \frac{\partial v^2 s}{\partial y} + \frac{\partial vus}{\partial x} = -h\frac{\partial \phi}{\partial y} + \nu r\left(\frac{\partial^2 v}{\partial x^2} + \frac{\partial^2 v}{\partial y^2}\right) + \nu v\alpha + g_y + MBY \tag{22}$$

where

$$MBY = -\frac{\partial}{\partial y}\left\{\frac{h}{3}(V_b^2 + V_bV_a + V_a^2)\right\} - \frac{\partial}{\partial y}(2vR_v) - \frac{\partial}{\partial y}\left\{\frac{h}{6}(2V_bU_b + V_bU_a + U_bV_a + 2V_aU_a)\right\} - \frac{\partial}{\partial x}(vR_u + uR_v) + \nu\left[\left\{\frac{\partial^2}{\partial x^2} + \frac{\partial^2}{\partial y^2}\right\}\left\{\frac{h}{2}(V_b - V_a)\right\}\right] \tag{23}$$

By incorporating the variation of u and v with respect to z into Equations (18) to (22), Equation (9) is essentially eliminated. The resulting equations completely define the flow in the region bounded by the two moving surfaces S1 and S2. The presence of these surfaces is manifested in h, r, s, and α, while their movement is depicted by MBC, MBX, and MBY.

Equations (18) to (23) are particularly suitable for the numerical solution of flow problems in a region bounded by two rigid surfaces of complex configuration. Both, the nature of the confining surfaces, as defined by $z = a(x, y)$ and $z = b(x, y)$, as well as their movement as defined by $U(x, y)$ and $V(x, y)$ have been maintained in general terms. When applied to the special case illustrated in Figure 1, the moving boundary terms MBC, MBX, and MBY simplify considerably. The curvature and movement of the surfaces S1 and S2 are symmetric about the x-y plane. V_a and V_b, the y-components of velocity at the confining surfaces, vanish. The x-components U_a and U_b are equal and a function of x only, that is, $U_a = U_b = U_w(x)$. Thus, Equations (19), (22), and (23) reduce to

$$MBC = \frac{\partial}{\partial x}(hU_w) \tag{24}$$

$$MBX = -\frac{\partial}{\partial x}(hU_w^2) - 2\frac{\partial}{\partial x}(urU_w) - rU_w\frac{\partial v}{\partial y} + \nu\frac{\partial^2}{\partial x^2}(hU_w) \tag{25}$$

and

$$MBY = -\frac{\partial}{\partial x}(rvU_w) \tag{26}$$

METHOD OF SOLUTION

Representation of the Fluid and the Computational Mesh

The Marker-and-Cell (MAC) method (Harlow and Welch, 1965) was chosen for the numerical calculations because of the presence of a free surface at the lateral fluid boundaries, whose position varies with time in a manner not known a priori. This method employs two coordinate systems.

The primary coordinate system covers the entire domain of interest with a rectangular grid of cells, each with dimensions δx and δy. The cells are numbered by indices i and j, with i counting the columns in the x-direction and j counting the rows in the y-direction. The field-variables values describing the flow are directly associated with these cells; their points of definition are shown in Figure 3. The indicated layout of the variables u, v, Φ, ψ, and D was chosen in the original MAC development to attain rigorous conservation of mass without involving cells beyond those which are contiguous to the cell of interest. The variables r, s, α, and h do not appear in the MAC arrangement; they are a consequence of the transformations carried out in the previous section. Their location within the cell was selected to match the position of the MAC variables. This arrangement which involves calculating two sets of values for each variable, one set located at cell centers and another at the grid center, was found to be stable and accurate.

The second coordinate system is that of the marker particles which describe the Lagrangian trajectories of the fluid elements. These particles delineate the location of the fluid surface. They move through a network of Eulerian cells which are flagged to denote whether they are empty (E), full and at the surface (S), or full and not adjacent to an empty cell (F). In addition, the network is sur-

rounded by a frame of boundary cells (B) which may also contain particles, in which case they are either inflow or outflow boundaries; or may be empty representing rigid walls. This labeling is illustrated in Figure 4. These particles contribute nothing to the dynamics. They enter the calculations only in that they determine the location and orientation of the free-surface, that is, the finite-difference equations are solved only in the region of the rectangular mesh that contains marker particles.

Finite Difference Solution

The quantity (Q), which is analogous to the vorticity in two-dimensional flow, is defined as

$$Q \equiv \frac{\partial}{\partial y}\left(\frac{ru}{b-a}\right) - \frac{\partial}{\partial x}\left(\frac{rv}{b-a}\right) \qquad (27)$$

In this case, however, Q is restricted to incompressible flow between two surfaces implicitly delineated by $a(x, y)$, $b(x, y)$, and $r(x, y)$ as described earlier. Just as in the usual vorticity equation, the equation for the transport of Q is independent of the pressure. Therefore, by inserting an arbitrary pressure field into Equations (20) and (22) a tentative velocity field which carries the correct values of the pseudo vorticity Q is obtained. The arbitrary pressure field will not, however, assure the vanishing of the discrepancy term D, defined as

$$\nabla \cdot \vec{V} = D \qquad (28)$$

However, if the tentative velocity field is corrected by the addition of the gradient of an appropriate potential function ψ, the pseudo vorticity Q remains unaltered and the true velocity field will be uniquely determined.

The finite-difference approximations (FDA) for Equations (18), (20), (22), and (27) are written in explicit (retarded-time) fluxes. Details are given by Hazbun (1971). The cell-centered terms for the convection of momentum are expressed in a special differencing code, referred to as ZIP-type. This technique eliminates negative diffusion-like truncation errors and ensures conservation of momentum at rigid boundaries (Hirt, 1968). Because the FDA for the momentum transport Equations (20) and (22) are explicit, the tentative velocity field can be determined directly. The calculation of the true velocity field must, however, be performed in such a way as to preserve the value of Q at every interior point and simultaneously

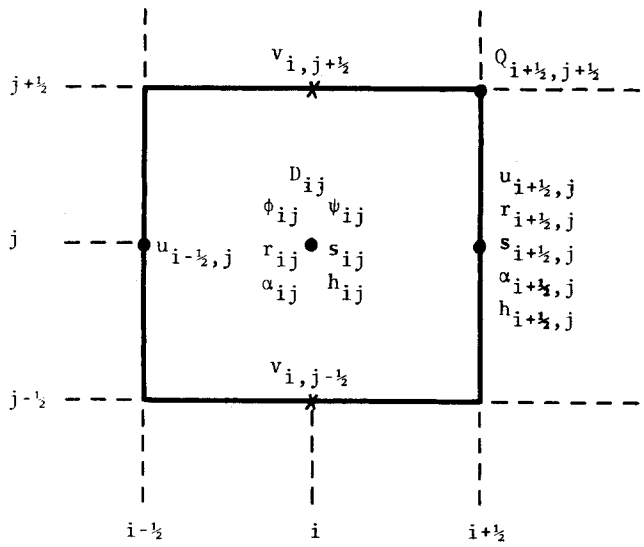

Fig. 3. Cell notation.

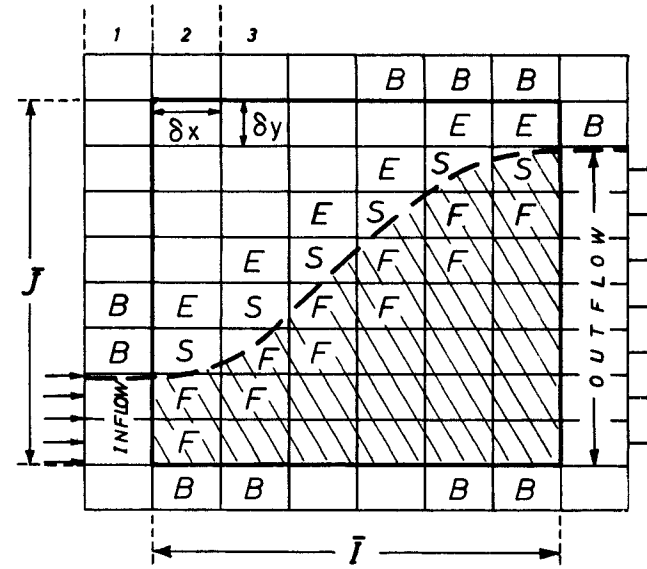

B = Boundary (Inflow, Outflow, Freeslip or Noslip)
E = Empty (No marker particles)
F = Full (Contains particles and is not adjacent to an Empty cell)
S = Surface (Contains particles but is exposed on one or more sides)

Fig. 4. Cell labels and computing mesh.

satisfy continuity. To achieve this, a corrective expression in terms of the space gradients of the potential function ψ is introduced. This results in a Poisson equation in ψ which must be solved prior to obtaining the final correct velocities. These final velocity components are calculated for all faces of F and S cells except for the exposed sides of S cells. On the mesh boundary, the change in velocity will be zero when $\psi_{\text{outside}} = \psi_{\text{inside}}$, except for continuative outflow boundaries where the velocity is adjusted by the gradient in ψ.

The final velocity components represent the velocity field relative to the moving surfaces and cannot as yet be used to move the marker particles. The true fluid velocity components relative to the Eulerian mesh are first calculated. The two-dimensional velocity field in any of the horizontal planes lying between the two moving surfaces S1 and S2 may be computed from Equations (10) and (11). For simplicity, however, only the central plane at which $f(z) = 1.0$ is considered, and the true velocity components u^t and v^t are calculated in this plane for all F and S cells. These velocities are then used to move the marker particles by means of an area-weighting scheme analogous to that devised by Amsden and Harlow (1970).

Sequence of Operations during a Computational Cycle

Prior to starting the cyclic advancement of the flow field, the problem is defined by specifying

(1) the shape, velocity and separation of the moving surfaces,

(2) the dimensions of the inflow region and the velocity profile of the incoming fluid. The inflow boundary is on the left side of the computational mesh. It may be as narrow as one cell or it may span the whole left side.

(3) the dimensions of the outflow boundary on the right side of the computational mesh. The outflow may be continuative or of prescribed velocity.

(4) the boundary conditions at the remaining sides of the rectangular Eulerian mesh. Free-slip is specified for a

line of symmetry or no-slip for a rigid wall.

(5) the initial fluid configuration within the mesh. This is set by means of marker particles. In the case of free-surface flows the region may be empty or partially full. For confined flows, the mesh is filled with fluid-marker particles.

The cells are flagged: (Inflow, Outflow, Free-slip or No-slip), and then the following sequence of events by which the configuration is advanced from one time-step to the next is performed.

1. The pressure and velocity fields within the fluid are know either as a result of the previous cycle of calculation or from the prescribed initial conditions which may be arbitrary.

2. Surface cell velocities on empty cell faces are forced to satisfy continuity [Equation (18)].

3. The pressure field is adjusted to satisfy the normal stress condition at the fluid surface as discussed later.

4. The velocities just outside the free surface are adjusted to satisfy the tangential stress condition.

5. The wall boundary conditions are used to set the tangential velocities across the walls.

6. A tentative velocity field of advanced-time velocities is calculated within the fluid using explicit FDA of Equations (20) and (22). The correct velocities at the boundaries ensure that this tentative velocity field contains the correct pseudo-vorticity Q at every interior point. The tentative velocities do not necessarily conserve mass.

7. Applicable values are set for ψ in all free surface and boundary cells.

8. The solution of the Poisson equation in ψ is performed through an iterative process that circulates among all full cells.

9. The final velocity field is then calculated by adding the x and y gradients of ψ to the corresponding components of the tentative velocity field.

10. Surface cell velocities are readjusted as in steps (2) and (3) to satisfy continuity and the tangential stress condition.

11. The across-the-wall tangential velocities are reset as in step (5).

12. The correct and complete velocity field calculated above is the two-dimensional field in the horizontal plane at which $f(z) = 1.0$ in Equations (10) and (11). It gives the velocity components relative to the moving surfaces. Equations (10) and (11) are therefore used to calculate the true velocity field relative to the Eulerian mesh.

13. The marker particles are moved according to the true velocity components in their vicinity.

14. Adjustments are made for the passage of marker particles across the cells and the inflow-outflow boundaries. The cell matrix is then reflagged completing one cycle of the calculations.

This sequence is repeated for as many time steps as desired. A few hundred cycles are usually needed to reach steady state.

Boundary Conditions

With the exception of the boundary conditions at the moving surfaces which were incorporated into the working equations the flow conditions at the lateral boundaries have not been defined. This is in accordance with the MAC method in which the numerical procedure is maintained as general and as flexible as possible with respect to boundary conditions. In addition to the moving boundaries this study is concerned with a prescribed set of rigid walls that may be no-slip or free-slip, inflow and outflow boundaries, and a free fluid surface whose position is transient. The rigid walls may partially confine the fluid in the lateral directions or may simply bound the computational mesh within which the fluid is laterally confined by a free surface that is independent of the rigid walls. Inflow boundaries have prescribed conditions of fluid influx through them, while outflow boundaries allow fluid outflux with minimal disturbance to the fluid remaining in the region of the calculations.

The requirement of zero momentum-flux across a free fluid surface forms the basis of the numerical formulation of the boundary conditions in all surface cells. The internal viscous stresses at the fluid surface are balanced against the external forces resulting in two sets of boundary conditions; one is applied normal to the surface and the other is tangential to the free surface. Clearly then, the exact application of these conditions requires an accurate knowledge of the free-surface location and orientation. This presents some difficulties which complicate the numerical procedure and force a compromise between accuracy and numerical complexity.

In the original MAC method (Harlow and Welch, 1965), the free surface boundary conditions were based on:

1. setting the velocity components in all surface cells so as to satisfy continuity.

2. equating internal surface pressure to applied pressure. This treatment does not give the proper viscous stress at the surface and is only valid if the coefficient of viscosity is sufficiently small. In this problem, which involves fluids of high viscosity, such conditions proved to be inadequate. They resulted in very uneven fluid surfaces that failed to represent the observed fluid behavior.

The need for careful utilization of the correct boundary conditions had been recognized by the Los Alamos group from the start; but the difficulties of applying these conditions were only recently resolved by Nichols and Hirt (1971). Their treatment is based on the inclusion of the correct tangential and normal, free-surface, stress conditions. This gave rise to a nonzero pressure at the center of surface cells which required delineating the fluid surface and appropriately adjusting the Poisson equation for pressure. Due to the different formulation in this study, the Poisson equation encountered is that for the potential function ψ rather than the pressure. This problem was overcome by the use of the pseudo-pressure field θ which had an arbitrary value within the fluid but the correct value in all surface cells. A scheme was then devised for calculating the correct pressure at the cell centers by interpolation from the values calculated at the fluid surface. This interpolation technique, which is described in detail by Hazbun (1971), depends on keeping a particle count in each cell which is updated at the end of each time-cycle. The interpolation factor is then estimated from the ratio of the number of particles in each surface cell to the average number of particles in the adjacent full cells.

NUMERICAL CALCULATIONS

The numerical procedure outlined above was coded for the IBM 360/75 system. A complete listing of the Fortran IV programs is given by Hazbun (1971). For illustrative calculations of the time-dependent flow in the configuration shown in Figure 1, the following form of the similarity function $f(z)$ defined by Equations (10) and (11) was selected:

$$f(z) = \frac{(b - z)(z - a)}{ab} \tag{29}$$

which is parabolic in z. For the symmetric case $a = b =$

$\pm h/2$, this reduced to

$$f(z) = \frac{(2z - h)(2z + h)}{h^2} \tag{30}$$

The expressions $r(x, y)$, $s(x, y)$, and $\alpha(x, y)$ defined in Equations (13), (14), and (17) were then evaluated in terms of $h(x, y)$ by appropriate integration or differentiation in the finite region $\pm h/2$. Initially, at $t = 0$, the flow region was empty of fluid and the moving surfaces were traveling at a constant linear velocity U. The velocity profile of the incoming stream was specified such that if the fluid inlet velocity were equal to that of the moving boundaries a uniform profile would be selected. On the other hand, if the inlet velocity were higher or lower than that of the belts, then a parabolic profile would be calculated to match Equation (30). This method of setting the inflow conditions eliminates the creation of a discontinuity in the velocity profile at the point of contact between the incoming fluid and the moving belts, which would otherwise lead to numerical instability. It is based on the premise that as soon as the fluid contacts the moving surface it adheres to it and therefore assumes the same velocity at the points of contact.

The flow conditions that were investigated covered a range of parameters of practical interest as summarized in Table 1. The conditions and results for two cases are summarized in Table 2. These cases illustrate the solution for two types of traveling surfaces: straight and elliptical-convergent.

Table 1. Range of Parameters Investigated

Kinematic viscosity	1.67-6.04 m²/s
Flow rate	0-0.101 kg/s
Linear speed of traveling surface	4.23-25.4 mm/sec
Terminal thickness of flow stream	2.54-7.62 mm
Terminal width of flow stream	0.371-1.524 m
Reynolds number, $u_m l/\nu$	0.0025-0.5
Euler number, $p_m/\rho u_m^2$	0.0002-0.5

Table 2. Conditions and Computational Criteria

	Case I	Case II
Type of moving surfaces	Straight	Elliptical
Velocity profile at inlet	Uniform	Parabolic
Inlet velocity at z = 0, mm/s	4.64	8.66
Linear speed of belts, mm/s	4.64	11.62
Stream width at inlet, m	0.1355	0.1355
Belt separation at inlet, mm	19.05	38.1
Flow rate, (kg/s) × 10²	1.64	5.04
Fluid viscosity, m²/s	6.04	3.02
Length of convergent section, m	0.406	0.864
Length of parallel section, m	0.1016	0.1524
Final stream width at outlet, m	0.457	0.914
Belt separation at outlet, mm	6.35	5.08
Grid cells for ½ of flow field (I, J)	22 × 17	22 × 17
Cell size, $\delta x \times \delta y$, mm	25.4 × 16.93	50.8 × 33.9
Time interval, δt, s	0.6	1.2
Over-relaxation parameters, λ_{opt}	0.28	0.43
Convergence criterion, ϵ	10^{-5}	10^{-5}
No. of marker particles at steady state	2840	1380
Elapsed time to reach steady state (s)	210	180
Total number of cycles calculated	400	170
CPU time, s	732	307

The majority of the computations were performed over one half of the flow field using a 17 × 22 grid. The total number of cells involved in the calculation depended on the initial flow conditions and varied from one time-step to the other. All 374 cells, however, had to be checked as to whether or not they contained fluid particles at every step of the calculation. The number of particles used to represent the fluid was maintained at an average of 8 particles per cell. Finer free-surface resolution was obtained when more particles were used per cell; however, this was coupled with an increase in core requirements and computation time. For the above grid-and-marker particle distribution, a computation took between 0.5 and 10.0 sec. per time-step, dependent on the amount of fluid in the system during that time step. A typical flow-development run required 600 sec. of computer time (CPU) to converge to the steady state condition. For the finer grid spacings the computations took a correspondingly longer time but, for the shorter time-steps, the increase in CPU time was moderated by the faster convergence of the successive-over-relaxation solution to the Poisson equation. The results obtained with the indicated grid and number of cells agreed to within 6% with the values obtained by extrapolating the grid size to zero.

Not all runs were started with no fluid in the system. Indeed, if only the final steady state was of interest, then a flow field approximating that expected at the steady state was constructed by introducing marker particles with the appropriate velocities into the computation mesh. By using the steady state flow configuration of one case as the starting conditions for a slightly different one, the number of time cycles required to reach the new steady state could be reduced to less than one quarter of those that would otherwise be required.

The relative convergence criterion ϵ for the Poisson equation was set at 10^{-5} for most runs. This value achieved rigorous conservation of mass in all cells, that is the divergence-discrepancy D rarely exceeded 10^{-6} for internal cells and 10^{-5} for surface cells. Useful results were, however, obtained with higher values of ϵ, for example, most of the trial runs used 10^{-3} or 10^{-4}. With these values the number of iterations required for convergence was more than halved.

The time-step δt also had a significant effect on the rate of convergence. For a given value of ϵ, halving δt decreased the number of iterations by approximately 60%; but, because the Poisson equation solution usually constituted less than 35% of the overall calculations per cycle, it was more economical to use as large a δt as allowable within the accuracy and stability requirements.

The most sensitive check for steady state convergence was found to be the relative change in the peak pressure from one time-step to the next. This may be expressed as

$$\epsilon_{ss} > \left| \frac{|\phi_p'| - |\phi_p|}{|\phi_p'| + |\phi_p|} \right| \tag{31}$$

A value of 10^{-3} for ϵ_{ss} was found adequate.

RESULTS AND DISCUSSION

Flow Characterization Results

The flow pattern developed during the passage of a fluid stream between two moving convergent surfaces establishes the pressure between these surfaces. Knowledge of the pressure profiles within the flow field is cru-

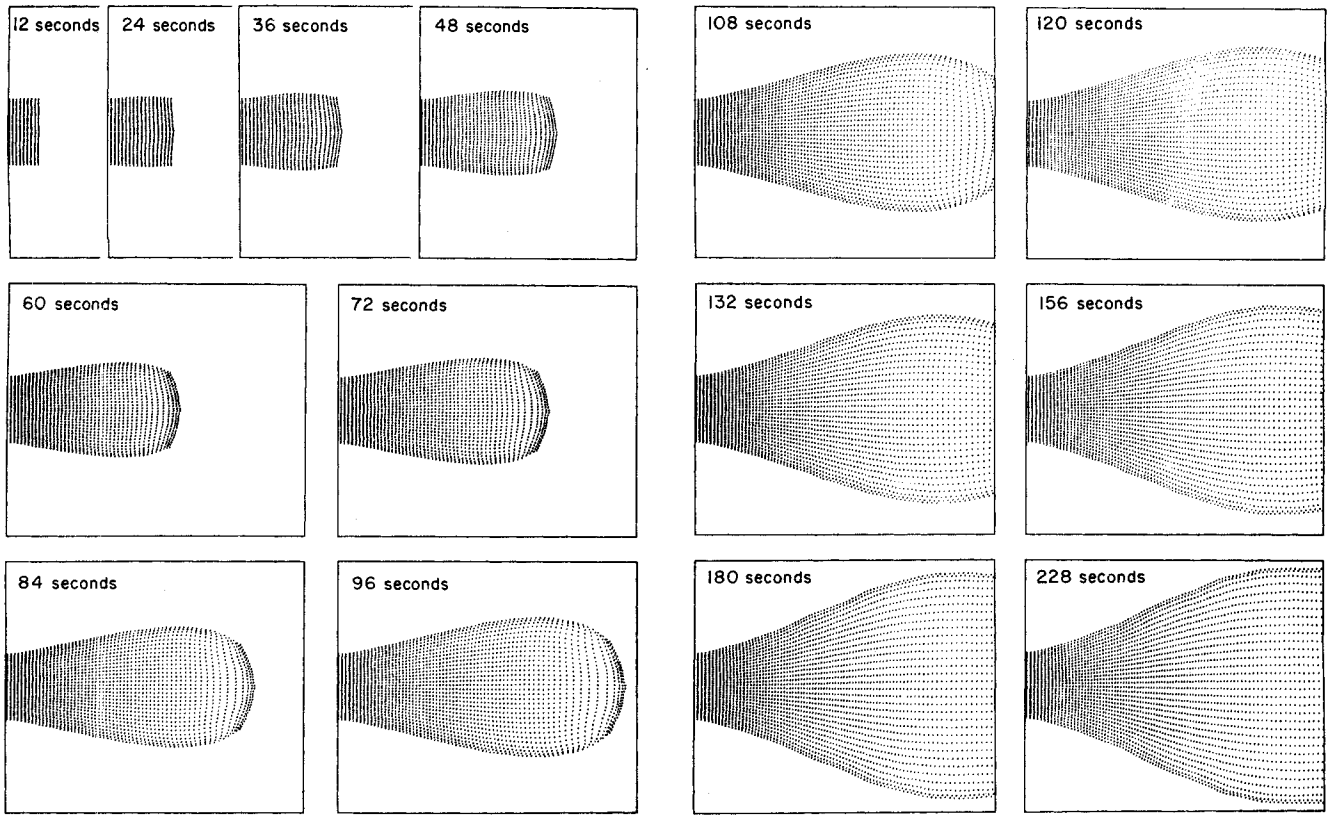

Fig. 5. Development of steady state laminar flow between two non parallel moving surfaces. Case I—Straight convergent surfaces.

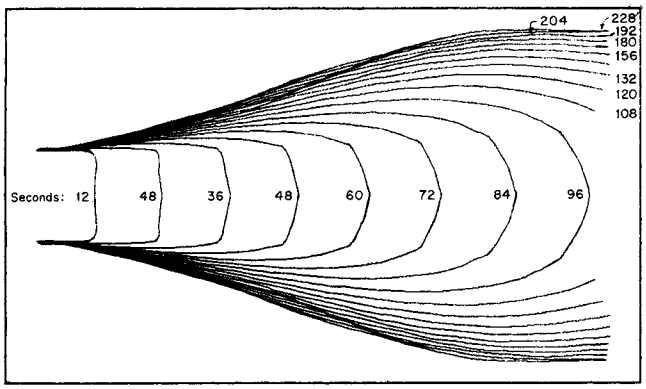

Fig. 6. Development of the free fluid surface. Case I—Straight convergent surfaces.

cial to the proper mechanical design of the sheetforming system. For this reason two complete flow-characterization cases are described in this Section and presented in Figures 5 to 16.

In Case I, straight convergent surfaces with a slope of 1:60 were considered; while, in Case II, elliptically curved surfaces with inlet and outlet separations of 38.1 and 5.08 mm, respectively, were studied.

For all the following graphs, the fluid was introduced at time $t = 0+$ into the system through a central section in the left hand side boundary. When the fluid reached the outflow boundary at the right hand side, it was removed from the system at a rate governed by the working equations.

To properly describe the flow patterns vast amounts of tabulated data listing all the cell variables are needed. Such data, however, cannot be easily interpreted and are almost useless in helping to visualize the flow pattern. For

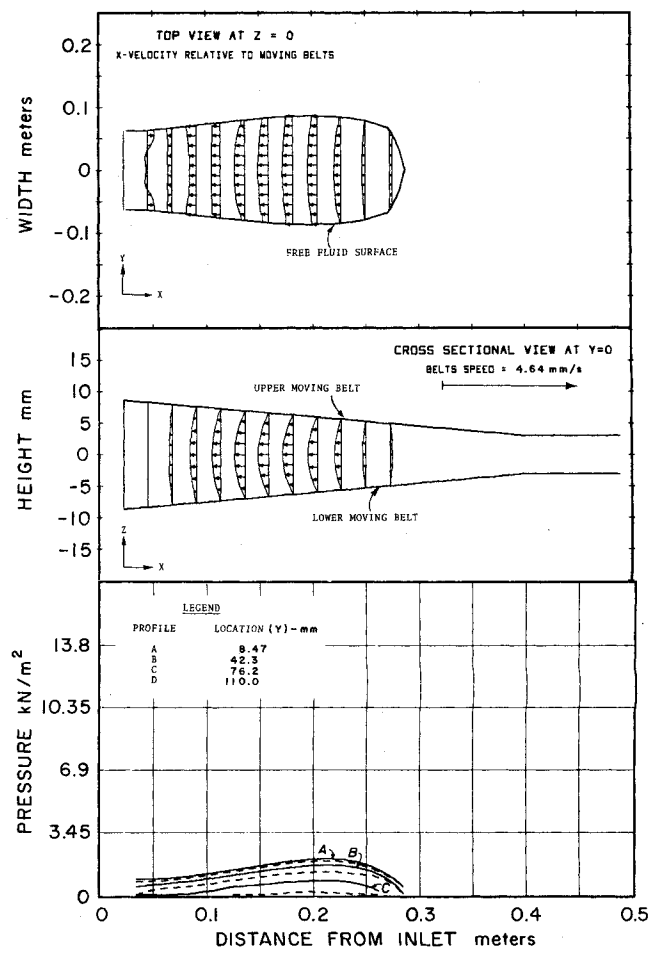

Fig. 7. Case I—Velocity distributions and pressure profiles at t = 60 sec.

this reason, the results are presented in several types of plots which follow.

Case I. Straight Convergent Surfaces

Figure 5 consists of a set of particle configuration plots, which were made by plotting the x and y coordinates of all the marker particles in the $z = 0$ plane, viewed from above the upper belt surface. These pictures show the relationship of the fluid to the system at a sequence of times during the development of the flow. The particles may be thought of as marking the instantaneous position of the fluid molecules in the system relative to the confining boundaries. Scanning vertically along the columns of inflow particles allows their interpretation as Lagrangian time-lines. The motion of the fluid could be simulated by projecting on a screen a sequence of these frames. This is impractical on a digital plotter but could be performed on a microfilm recorder. In Case I, 400 time-cycles were calculated; therefore, an equivalent number of such plots could have been generated.

Figure 6 depicts the location of the free-fluid boundary at several time-steps. The slow approach to steady state can clearly be seen as the elapsed time t exceeds 180 seconds. In the computer program the normal and tangential stress conditions of the free surface were applied at angles of 0, ±45°, ±90°, ±135°, or ±180°. The effect of this approximation on the free fluid boundaries is apparent in Figure 6. In this case, where the sloping regions of the boundary have a true angle of ±30° to ±40° to the horizontal (x-axis), the stress conditions were applied at 0° in some cells and ±45° in others resulting in the slight waviness that can be seen in the free boundary.

Figures 5 and 6, although assisting visualization of the flow, do not provide quantitative information on the flow field. Such data are presented in Figures 7 to 10. These plots give a complete set of velocity distributions and pressure profiles at the indicated elapsed times. The values in Figures 7 to 10 were plotted exactly as computed without any smoothing. Each figure consists of three parts drawn on the same x-scale. The upper two parts represent the distributions of the x-component of velocity in the y and z directions respectively, all velocities being shown relative to the moving belts. The lower part gives the pressure field in the system in the form of pressure profiles at different values of y. The magnitude of the velocity vectors in both velocity plots may be determined by comparing their lengths with that of the velocity vector for the moving belts given in the middle plot. A study of Figures 7 to 10 gives a clear picture of the flow pattern, the magnitude of the velocities encountered, the pressures generated, and the nature of the flow. From these plots it may be concluded that initially the fluid is conveyed forward by a combination of shear pressure and inertial flow. The drag and inertial flow tend to move the fluid in the x-direction while pressure spreads the fluid laterally. As the separation between the moving belts narrows, pressure flow dominates and the fluid is essentially pumped into the parallel section of the traveling surfaces. The transition from drag flow to pressure flow takes place at a short distance (38 mm in Case I) from the point where the

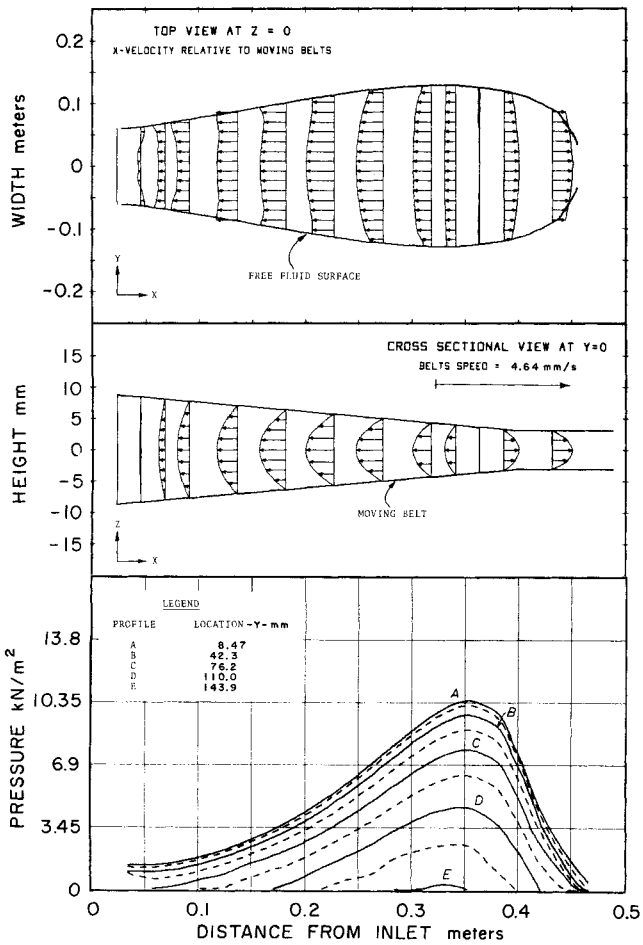

Fig. 8. Case I—Velocity distributions and pressure profiles at t = 96 sec.

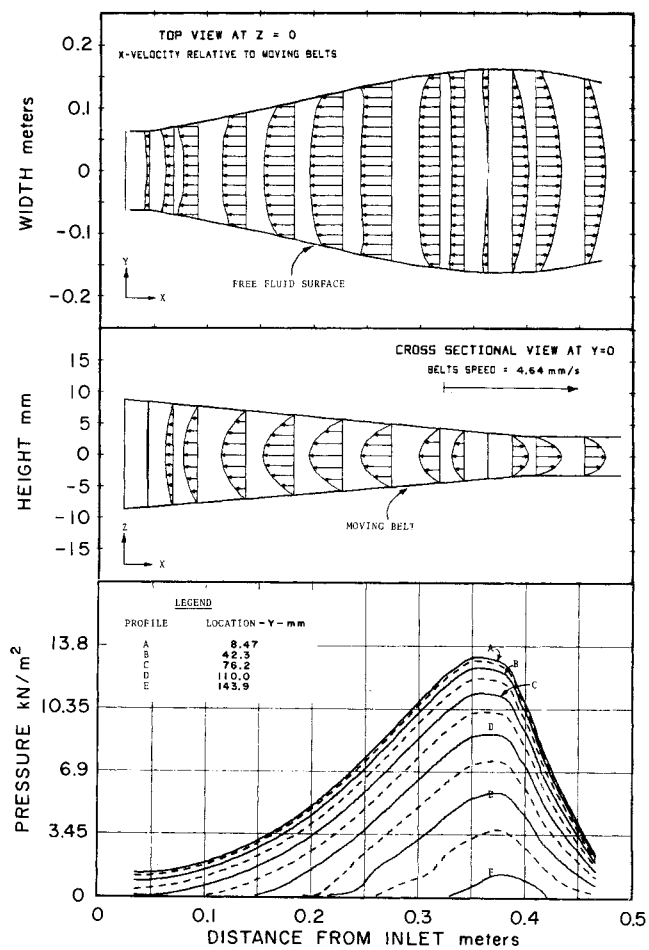

Fig. 9. Case I—Velocity distributions and pressure profiles at t = 120 sec.

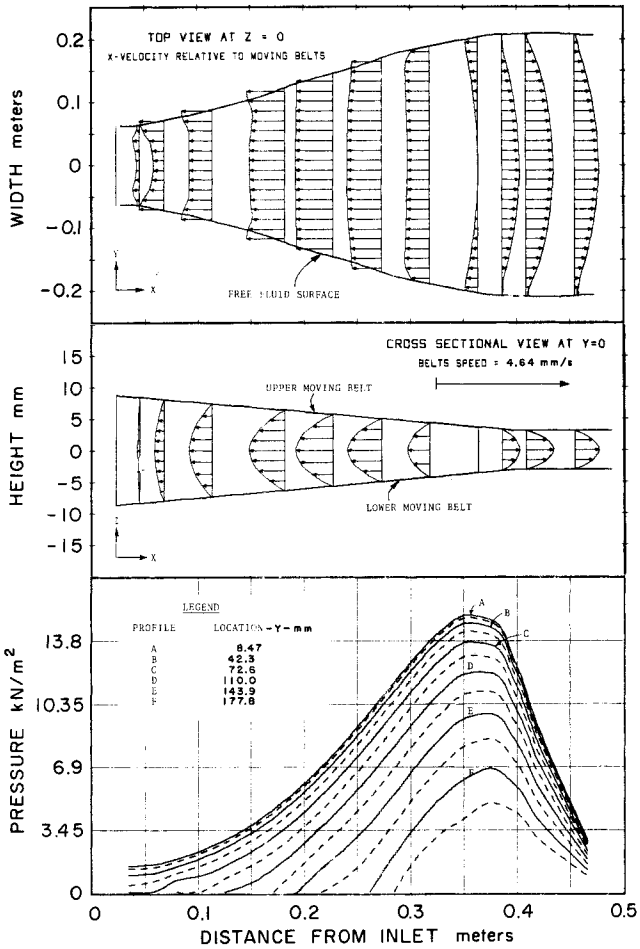

Fig. 10. Case I—Velocity distributions and pressure profiles at t = 180 sec.

belts become parallel. This transition is marked by a peak in the pressure profiles and a reversal in the direction of the flow relative to the moving belts. The fluid stream flows into the parallel section at an average forward velocity higher than that of the traveling surfaces. This excess velocity gradually decreases as the fluid stream approaches the outflow boundary.

Case II. Elliptically Curved Surfaces

No particle configuration plots are presented for Case II. The development of the free fluid boundary is shown in Figure 11 at less frequent intervals than in Case I to allow easy interpretation. The same waviness may be seen in the sloping parts of the free surface as that observed in Case I. The stream in this case is made to spread to 0.914 m, twice as wide as in Case I.

Figures 12 to 15 depict the same general flow behavior although considerably higher pressures are generated. In this case, the transition from drag flow to pressure flow occurs at 0.178 m from the end of the convergent position, which is twice the distance observed in Case I relative to the dimensions involved. This is due to the different curvatures of the moving boundaries. It is significant to note that the peak in the pressure profiles does not exactly coincide with the point at which the reversal in the flow relative to the belts takes place. A probable explanation is that at the much higher velocity and lower viscosity inertia may be significant enough to cause the difference in the location of the pressure peaks. The decrease in the velocity on reaching the parallel section is more gradual than in Case I. This is most likely due to the larger stream width and lower thickness. Readjustments in the flow appear to take place first at the edges of the stream and then propagate to the center. Thus for a wide stream the decrease in the average velocity within the parallel section occurs more gradually than for a narrower but thicker stream.

Finally, the difference in the flow pattern at the inlet is significant. The fluid stream entered the system in Case I at a uniform velocity; it quickly readjusted to a parabolic profile as seen in Figure 9. In Case II, as shown in Figure 13, the inlet fluid stream possessed the correct profile but had an average velocity that was too low to match the

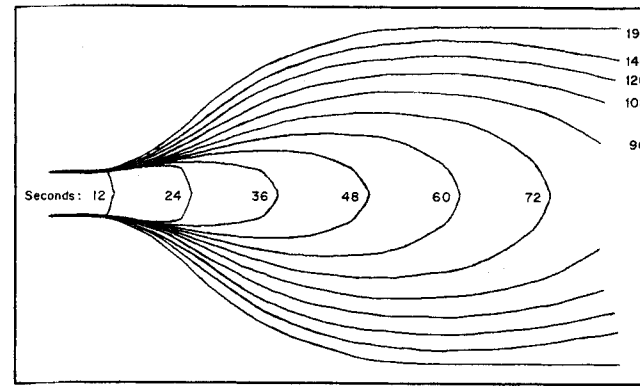

Fig. 11. Development of the free fluid surfaces. Case II—Elliptically curved surfaces.

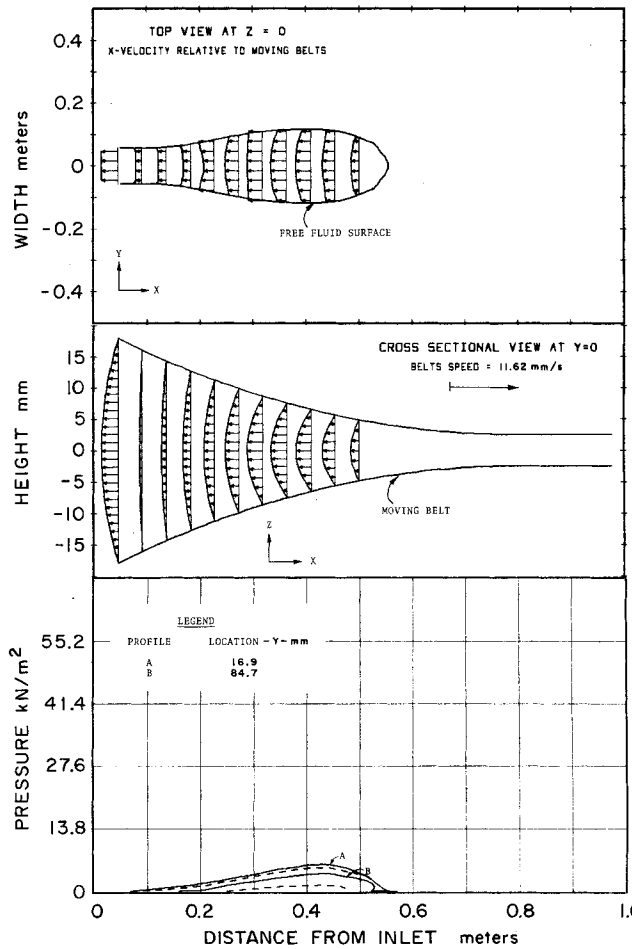

Fig. 12. Case II—Velocity distributions and pressure profiles at t = 48 sec.

flow conditions, resulting in a slight necking of the fluid stream. This decrease in width disappeared as steady state was approached as indicated in Figure 14.

The flow conditions at the inlet do not appear to influence the flow far downstream. The difference in the inlet velocity relative to the belts is clearly reflected in all the pressure profiles of Case II. A comparison of the pressure traces of Case I with those of Case II reveals that the pressures generated in the entrance region, when scaled to the corresponding peak values, are considerably lower in Case II than in Case I. This difference, however, extends only two to three inlet-widths downstream.

Figure 16 shows the lateral (y-direction) velocity profiles for three time-intervals as the flow approaches steady state. The y-velocity field was calculated for each case but is presented here only for Case II. The profiles show that lateral flow initially takes place throughout the flow field. When the steady state is reached ($t = 3.2$ min.), most of the lateral spreading takes place in the first two-thirds of the flow field. The magnitude of the lateral flow at certain parts of the free surface exceeds half that of the forward velocity of the belts. The magnitude of the velocity vectors may be determined by comparison with the scale vector in the top left-hand corner of each plot.

Confirmation and Application of Results

The second invariant of the rate of deformation tensor was calculated for the steady state to evaluate the assumption of Newtonian behavior. This quantity varied from 0.00015 to 0.0085 sec.$^{-2}$ for Case I and from 0.0026 to 0.055 sec.$^{-2}$ for Case II.

Good agreement of the computed pressures and centerline velocities and experimental values for Case I was demonstrated by Hazbun (1971). This comparison and the application of the computer program to the mechanical design of a system for the forming of plastic sheets will be presented in a subsequent paper.

ACKNOWLEDGMENT

The authors gratefully acknowledge the support granted for this research by the Rohm and Haas Company. They are also indebted to Dr. Francis W. Harlow who made several valuable suggestions that facilitated the application of the Marker-and-Cell numerical technique.

NOTATION

a = function defining location of lower moving surface: $z = a(x, y)$, m

b = function defining location of upper moving surface: $z = b(x, y)$, m

D = discrepancy term, $D = \nabla \cdot \vec{V}$, s^{-1}

$f(z)$ = similarity transformation function, defined by Equations (10) and (11), dimensionless

$\vec{g}$ = gravitational force, m/s^2

h = vertical separation between moving surface, m

l = width of fluid stream at exit, m

p_m = peak pressure, N/m^2

Q = pseudo vorticity defined by Equation (27), s^{-1}

R_u, R_v = functions defined by Equations (15) and (16), m^2/s

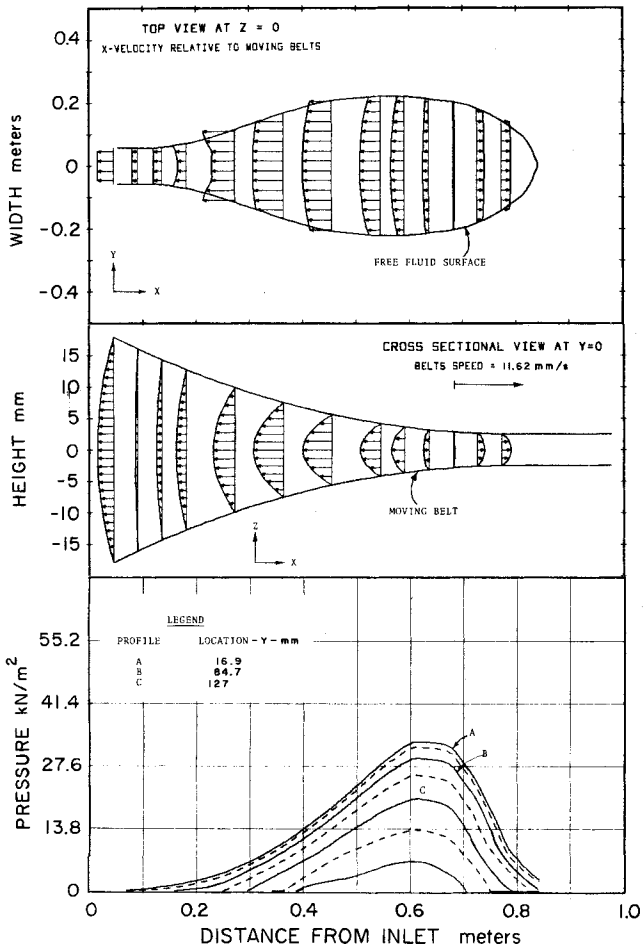

Fig. 13. Case II—Velocity distributions and pressure profiles at t = 96 sec.

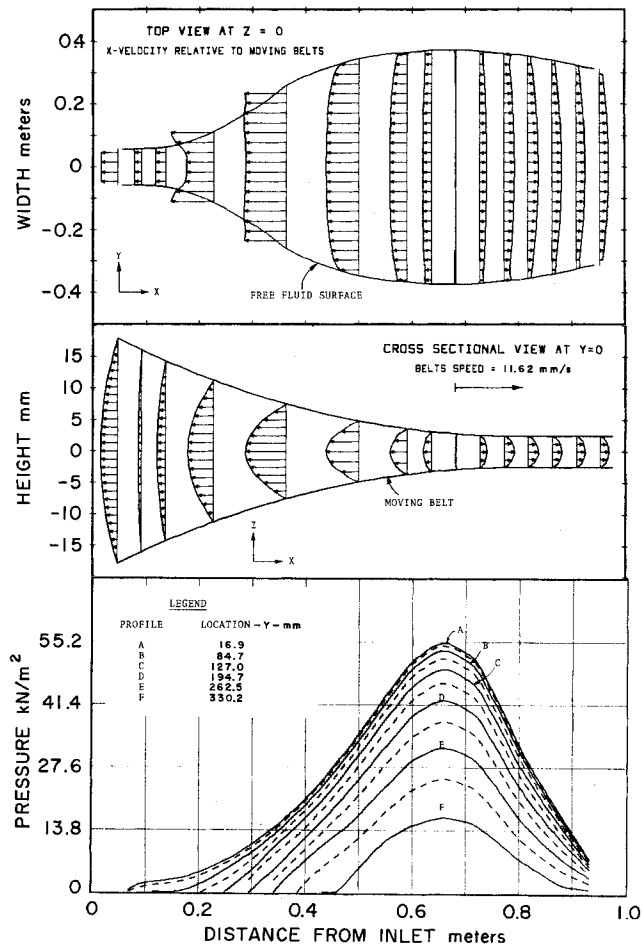

Fig. 14. Case II—Velocity distributions and pressure profiles at t = 120 sec.

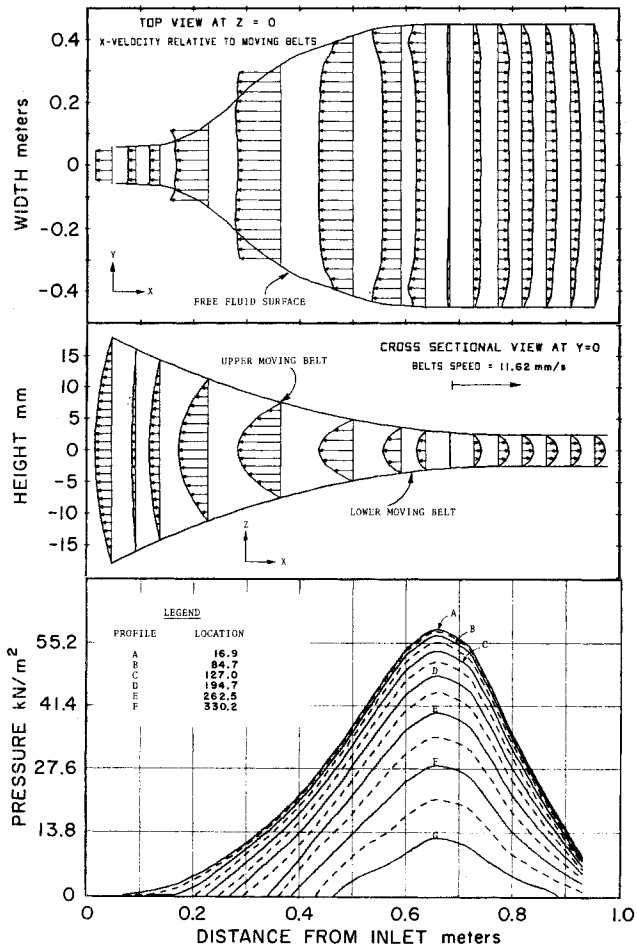

Fig. 15. Case II—Velocity distributions and pressure profiles at t = 192 sec.

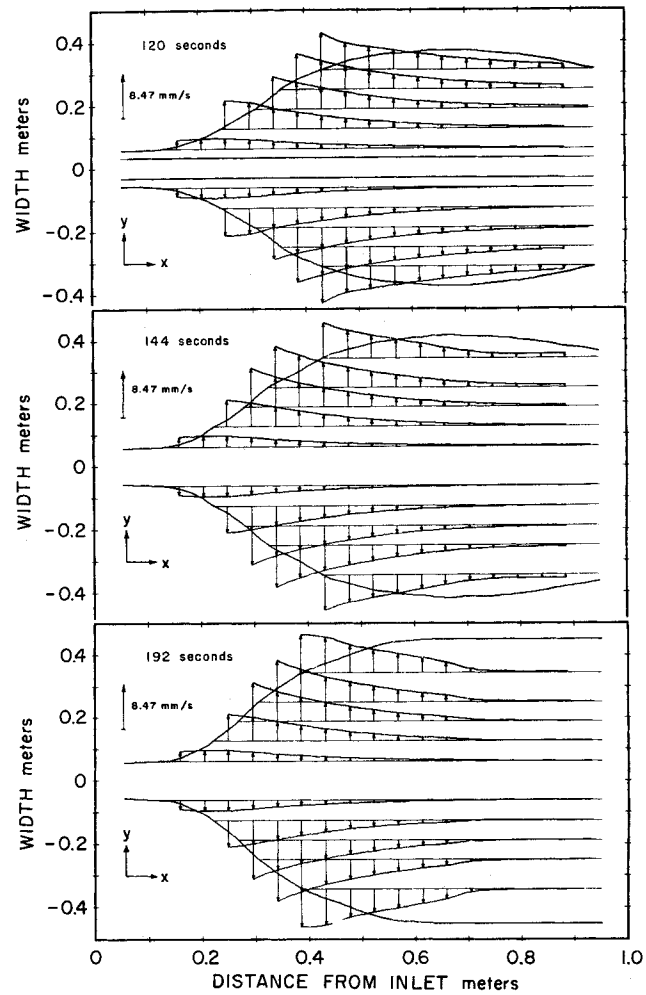

Fig. 16. Case II—Lateral velocity profiles at $Z = 0$.

r = integral of $f(z)$ in the range $z = a$ to b, m
S1 = lower moving surface defined by $z = a(x, y)$, m
S2 = upper moving surface defined by $z = b(x, y)$, m
s = integral of $f(z)^2$ in the range $z = a$ to b, m
t = time, s
U = velocity component of one of the moving surfaces in the x-direction, m/s
u = horizontal velocity component of the fluid relative to that of the moving surfaces, m/s
u_m = maximum value of u, m/s
$\vec{V}$ = fluid velocity vector with Cartesian components u, v, and w, m/s
V = when subscripted with a or b indicates the velocity component, of one of the moving surfaces, in the Y-direction, m/s
v = lateral velocity component of the fluid relative to that of the moving surfaces, m/s
w = vertical velocity component of the fluid in the z-direction, m/s
X, x = Cartesian coordinates, horizontal direction, m
Y, y = Cartesian coordinates, lateral direction, m
Z, z = Cartesian coordinates, vertical direction, m
α = friction term defined by Equation (17), m^{-1}
δ = finite difference increment, dimensionless (for example, δx, δy)
ϵ = convergence criterion $|(|\Phi^n| - |\Phi^{n+1}|)/(|\Phi^n| + |\Phi^{n+1}|)|$, dimensionless
ϵ_{ss} = convergence criterion for steady state, defined by Equation (31), dimensionless
θ = arbitrary hydrostatic pressure, used as initial estimate of Φ, N·m/kg
μ = viscosity N·s/m²
ν = kinematic viscosity, m²/s
ρ = density, kg/m³
Φ = hydrostatic pressure (p/ρ), N·m/kg
ψ = potential function, s^{-1}

LITERATURE CITED

Amsden, A. A., and F. H. Harlow, "The SMAC Method: A Numerical Technique for Calculating Incompressible Fluid Flows," *J. Computa. Phys.*, **6**, 322 (1970).

Bortnick, N. M., E. A. Hazbun, and J. W. White, "Double Belt Plastic Sheet Forming and Take-off System," U.S. Patent Application 31704, Rohm and Haas Co. (1970).

Harlow, F. H., and J. E. Welch, "Numerical Calculation of Time-Dependent Viscous Incompressible Flow of Fluid with Free Surface," *Phys. Fluids*, **8**, 2182 (1965).

Hazbun, E. A., "Three Dimensional Viscous Flow Between Convergent Traveling Surfaces," *Ph.D. thesis*, Univ. Pennsylvania, Phila. (1971).

Hirt, C. W., "Heuristic Stability Theory for Finite-Difference Equations", *J. Computa. Phys.*, **2**, 339 (1968).

McIntire, L. V., and W. R. Schowalter, "Hydrodynamic Stability of Viscoelastic Fluids," *AIChE J.*, **18**, 102 (1972).

Nichols, B. D., and C. W. Hirt, "Improved Free Surface Boundary Conditions for Numerical Incompressible-Flow Calculations," *LA-DC-12537 (Preprint)*, Los Alamos Scientific Lab. (1971).

Manuscript received September 12, 1972; revision received and accepted December 27, 1972.